

Full Length Article

Ethanol gas sensing mechanisms of p-type NiO at room temperature

Javier Bartolomé^{*}, María Taño, Ruth Martínez-Casado, David Maestre^{*}, Ana Cremades

Department of Materials Physics, Universidad Complutense de Madrid, Plaza Ciencias 1, 28040 Madrid, Spain

ARTICLE INFO

Keywords:

Nickel oxide
 Conductometric gas sensing
 Charge transfer
 Adsorption
 Electron backscattered diffraction

ABSTRACT

Conductometric gas sensors based on metal oxide semiconductors (MOS) usually require high temperature operation, increasing their energy consumption and limiting their applicability. However, room temperature operation with these devices still remains a challenge in many sensor-analyte systems due in part to the low or null response and recovery speeds obtained at this temperature. In this work, the conductometric response of p-type NiO ceramic samples to ethanol is studied under room temperature operation. An anomalous response consisting in an unexpected resistance decrease upon ethanol exposure is observed depending on sample texturing, which is tuned by changing the temperature at which the samples are synthesized. This anomalous response is characterized by fast response and recovery times. A model based on two competing mechanisms, consisting in either an electron transfer from NiO to the ethanol molecule or the catalytic decomposition of adsorbed ethanol, is proposed to explain the observed anomalous response. Extending this model to other MOS could pave the way for fast sensors operating at room temperature.

1. Introduction

Conductometric or chemiresistive gas sensing has been an active research area for several decades, with metal oxide semiconductors (MOS) standing out as one of the most relevant material systems since they were initially proposed for this application in the 1960s [1]. However, a renewed interest has raised over the last years due to the development and settlement of thin film technologies and the appearance of novel synthesis routes for the fabrication of nanostructured materials. MOS-based conductometric gas sensors are usually characterized by high sensitivities, low production costs and high robustness which has led to their widespread use, from industrial manufacturing to security or environmental monitoring [2,3]. The extremely high surface-to-volume ratio achieved in their nanostructured counterparts improved their sensitivities and response times even further [4–6]. Nevertheless, conductometric gas sensors still present some obvious flaws, which are their usually poor selectivity, high operating temperature, and their tendency to present temporal drifts that requires periodic calibrations [3,7]. In particular, the requirement to operate at high temperature implies a higher power consumption that in practice limits the functionality of these sensors [8]. Despite the long historical development of conductometric gas sensors, there are still open questions related to their fundamental working principle that need to be resolved in order to

develop new strategies capable of tackling these problems. Generally speaking, any conductometric gas sensing mechanism can be regarded as a charge injection/extraction process caused by the interaction between the analyte and the sensor surface, which in turn modifies the overall conductivity of the sensor. The specific mechanisms can be very varied, including direct charge transfer between the analyte and the sensor surface [9], formation of electronic depletion/accumulation layers on the sensor [10,11], catalytic decomposition of the analyte [12], redox reactions between the analyte and the sensor [13], or competition for adsorption sites [14], among others. Each mechanism may produce a different response in the sensor, sometimes leading to opposite behaviors for the same sensor-analyte system, depending on their nature. Since usually more than one mechanism is present during the whole sensing process, sometimes unexpected or contradictory results may be obtained depending on the sensing conditions or particularities of the fabricated device [15,16]. Unfortunately, this complex picture is usually ignored and most of the times the observed response is ascribed to an oversimplified process involving either redox reactions or ionosorption of oxygen species. The reason for this is the high dependence of the conductivity of metal oxides on adsorbed oxygen and oxygen defects, which makes these two options good candidates to explain those responses that match the expected behavior. However, failing to properly identify the possible sensing mechanisms involved in the

^{*} Corresponding authors at: Department of Applied Physics, Universidad Autónoma de Madrid, C/Francisco Tomás y Valiente 7, 28049 Madrid, Spain (J. Bartolomé). Department of Materials Physics, Universidad Complutense de Madrid, Plaza Ciencias 1, 28040 Madrid, Spain (D. Maestre)

E-mail addresses: javier.bartolomev@uam.es (J. Bartolomé), dmaestre@ucm.es (D. Maestre).

<https://doi.org/10.1016/j.apsusc.2021.152134>

Received 15 October 2021; Received in revised form 25 November 2021; Accepted 3 December 2021

Available online 8 December 2021

0169-4332/© 2021 The Authors.

Published by Elsevier B.V. This is an open access article under the CC BY-NC-ND license

(<http://creativecommons.org/licenses/by-nc-nd/4.0/>).

observed response may limit the recognition of potential applications and opportunities to overcome the typical limitations of these devices.

Contrary to most binary and transition metal oxides usually employed in conductometric gas sensing, such as SnO_2 , In_2O_3 , ZnO or TiO_2 [8,17,18], NiO is a p-type MOS. P-type oxides have been, by far, less explored as conductometric gas sensors compared to their n-type counterparts [19], and their different interaction with oxygen and oxygen defects may lead to different behaviors that can be exploited to fabricate new sensors with improved capabilities or enhance the response of n-type materials by the formation p-n heterojunctions. NiO has shown to have a good conductometric response towards ethanol, as published in a number of previous works [12,20–26]. Most of these works attribute the observed response to the decomposition of the ethanol molecule that reacts catalytically with the ionized oxygen species adsorbed on the NiO surface following the general reaction:



where subsequent reactions with other adsorbed oxygen species may further oxidize the obtained subproducts, thus reducing the concentration of holes in the surface. This assumed response mechanism suggests essentially strategies focused on increasing the porosity and surface-to-volume ratio of the samples, as a potential way to improve both the sensitivity and the response/recovery time of the devices [12,21], as well as the incorporation of dopants or the functionalization with other MOS to improve the reactivity of the surface or enhance the formation of accumulation/depletion layers [20,22–24,26]. However, if only this sensing mechanism is considered, reducing the operation temperature down to room temperature may appear as a bad strategy since the aforementioned decomposition reaction is favored at high temperatures. As will be shown in this work, fast room temperature ethanol gas sensing with NiO is actually feasible by virtue of a hereinafter called anomalous sensing mechanism, which is enhanced at this temperature depending on the morphology and crystalline surface orientation of the samples. For this study NiO ceramic pellets were synthesized by direct oxidation of compacted Ni powders in oxygen poor conditions, which allows us to tune the final grain size and morphology of the obtained samples [27]. The overall crystalline orientation of the exposed surface of the samples was correlated with their surface electronic and chemical properties, and the observed sensing behaviors. With the help of Density Functional Theory (DFT) calculations a model based in two competing sensing mechanism is proposed to explain the sensing response.

2. Methods and experimental section

All NiO samples were grown using metallic Ni powders (Sigma Aldrich 99.99 %) as precursor material. The initial Ni powders were compacted into pellets and annealed at different temperatures ranging from 800 to 1400 °C for 10 h under an Ar flow in order to keep a controlled atmosphere. In this work we will focus on two different NiO samples referred to as #800 and #1400 based on the corresponding annealing temperature. Structural characterization of the samples was performed by X-ray diffraction (XRD) in a Philips X'Pert Pro diffractometer using $\text{Cu K}\alpha$ radiation ($\lambda = 1.54158 \text{ \AA}$) in Bragg-Brentano configuration. Morphological study was carried out by scanning electron microscopy (SEM) using a Leica 440 Stereoscan and a FEI-Inspect S50. For the compositional analysis, energy dispersive X-ray spectroscopy (EDS) measurements were performed with a Bruker AXS 4010 detector mounted on a Leica 440 SEM. A Bruker e-FlashHR electron backscattered diffraction (EBSD) system attached to a FEI-Inspect SEM was used to obtain the orientation maps of the samples, employing an electron energy of 20 keV. X-ray photoelectron spectroscopy (XPS) measurements were carried out at the ESCA beamline at the Elettra synchrotron facility in Trieste (Italy). An excitation energy of 640 eV, with a spectral resolution of 200 meV, and a lateral resolution of 120 nm, was used. Binding energy calibration of the samples was performed

using the C (1 s) core level (285 eV) from residual carbon. Fitting of the obtained core level peaks was performed using Voigt profiles and Shirley background correction.

Gas sensing measurements were performed using a homemade set-up, schemed in Fig. S1, which allowed us introducing controlled amounts of ethanol gas by bubbling N_2 gas (99.999% purity) through liquid ethanol. The ethanol to N_2 ratio was regulated using a needle valve before the bubbler and mixing the resulting saturated ethanol + N_2 solution with pure N_2 . The sample chamber, with the loaded sample, is purged for 20 min before each experiment, and for 10 min between each ethanol exposure cycle using pure N_2 . Ethanol induced resistance changes were measured using a Keithley 2400 SourceMeter. Throughout this work, sensitivity is defined as the percentage ratio $\Delta R/R_0$, which are the sample resistance difference with and without ethanol, and the sample resistance without ethanol, respectively. Sensitivity curves have been corrected to account for the resistance drift of the samples by subtracting a polynomial baseline after each purge. Due to the bulky nature of the samples (ceramic pellets), a large concentration of 16,000 ppm of ethanol was used in these experiments, in order to obtain a clear response. However, similar behaviors were observed at lower ethanol concentrations (which may be reduced in our system down to ~200 ppm).

DFT calculations have been performed using the CRYSTAL program [28], in which the crystalline orbitals are expanded as a linear combination of atom-centered Gaussian orbitals, the basis set. The Ni, O, C and H ions are described using all-electron basis sets contracted as s(8) sp(6411) d(41), s(8) sp(411) d(1), s(6) p(311) d(1), s(511) p(1), respectively. Electronic exchange and correlation were approximated by using the Heyd-Scuseria Ernzerhof (HSE) hybrid functional. In order to avoid lateral interaction between ethanol molecules, 4 layers and a (4×4) supercell have been considered for all the studied surfaces. The internal coordinates have been determined by minimization of the total energy within an iterative procedure based on the total energy gradient calculated with respect to the nuclear coordinates. Convergence was determined from the root-mean-square (rms) and the absolute value of the largest component of the forces. The thresholds for the maximum and the rms forces (the maximum and the rms atomic displacements) have been set to 0.00045 and 0.00030 (0.00180 and 0.0012) in atomic units. Geometry optimization was halted when all four conditions were satisfied simultaneously. Several positions of ethanol, both on molecular and dissociated adsorption, have been considered to find the lowest in energy.

3. Results and discussion

After the thermal treatments carried out at 800 °C and 1400 °C, two different samples are obtained showing distinct morphological and microstructural features. Sintering effects are observed on sample #800 (Fig. 1a) which presents a surface formed by agglomerated grains with spherical shape and diameters in the range of few microns. Conversely, treatments carried out at 1400 °C result in the growth of densely packed, highly oriented microcrystals with dimensions ranging from 20 to 40 μm and faceted surfaces that develop well-defined terraces and arrays of squared shaped pits, as shown in Fig. 1b. These pits are inverted pyramids with exposed $\{111\}$ facets that grow on top $\{100\}$ surfaces along $\langle 011 \rangle$ directions [27]. XRD measurements confirm that the analyzed samples are formed by NiO with cubic structure (space group $Fm-3m$) and lattice parameters $a = b = c = 4.17 \text{ \AA}$ (Fig. 1c). Peak intensity distribution of sample #800 confirms its polycrystalline nature and random orientation, in agreement with the observed morphology. However, sample #1400 is strongly textured along the $\{100\}$ planes as evidenced by the enhanced intensity of its 200 reflection. It is worth noting that XRD measurements in Bragg-Brentano configuration only indicate the general crystalline orientation of the sample relative to the plane defined by its overall surface, not the actual orientation of the exposed surface: only on perfectly smooth and flat surfaces both

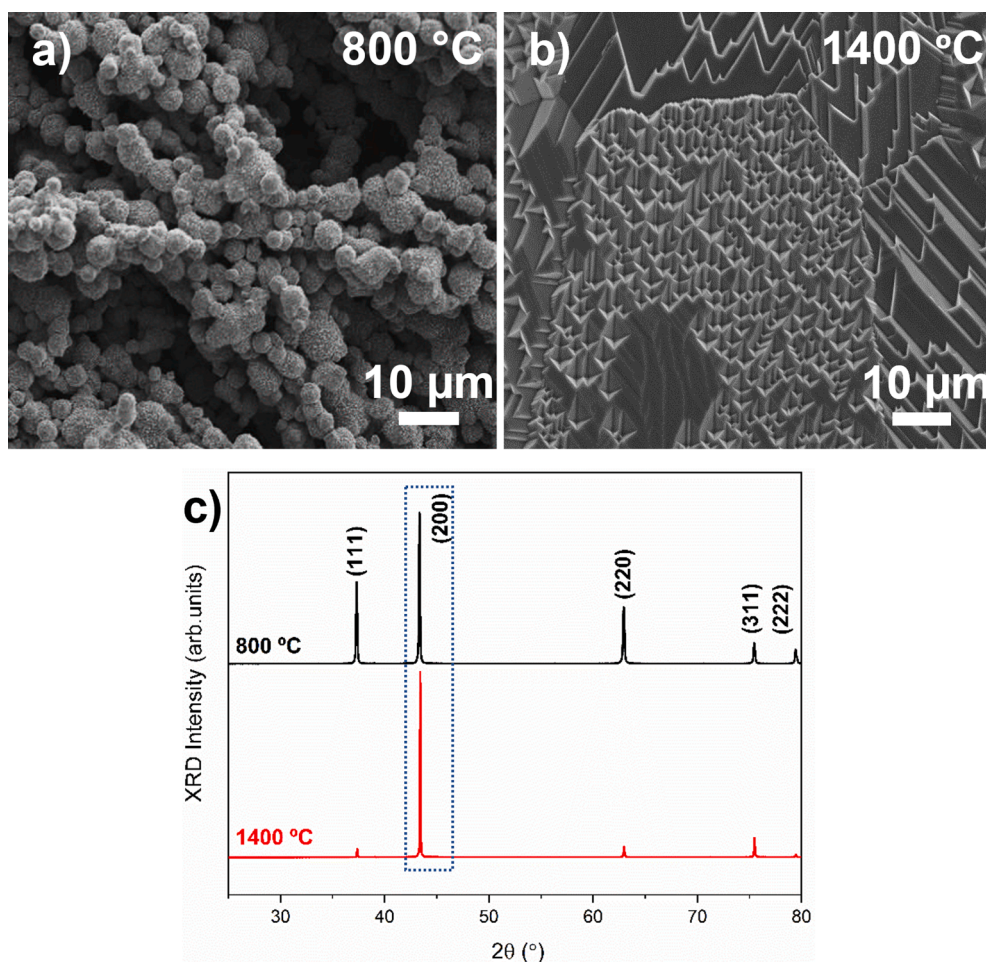


Fig. 1. SEM images of NiO samples sintered at (a) 800 °C and (b) 1400 °C. (c) Corresponding XRD patterns.

parameters will be the same.

The crystalline orientation of the exposed surfaces strongly affects their catalytic activity, their chemical reactivity and their adsorption energy barriers, thus being a relevant parameter to understand the sensing characteristics of the samples. Sample #800 has a completely random surface orientation as shown by the combination of SEM and XRD measurements. Sample #1400, on the contrary, is highly textured and presents large grains with well-defined facets, terraces and pits, thus pointing to a preferential orientation of its exposed surfaces. If the surface of the grains was completely flat and parallel to the sample surface, this preferential orientation will correspond to the $\{100\}$ planes as revealed by XRD. However, the exposed surface of terraces and pits, which essentially cover the majority of the sample surface, have different orientations. To elucidate their actual orientation, EBSD maps were performed on selected regions and the obtained pole figures are shown in Fig. 2. Fig. 2a shows a detail of one of those areas, which is representative of regions containing both pits (red arrow) and terraces (green arrow). The resulting crystallographic orientations for different family planes are shown in the pole figures plotted in Fig. 2b. Pits develop on $\{100\}$ surfaces, which is evident by the appearance of a central spot in the $\{100\}$ pole figure, and hence their internal facets correspond to $\{111\}$ planes, as reported in previous works [27]. Thus, the exposed surface of those grains which are completely covered by pits is oriented along the $\{111\}$ planes, despite their general orientation being the $\{100\}$. Fig. 2c shows the complete orientation schematic for the pits. Terraces, on the other hand, always develop parallel to $\{111\}$ planes, as indicated by the central spot in the corresponding pole figure of Fig. 2b, with the step wall parallel to either $\{100\}$ or $\{112\}$ planes

(see schematic of Fig. 2d). This is a general result obtained in all terraces measured by EBSD, which showed orientations compatible with $\{111\}$ exposed surfaces regardless of their tilting or rotation. Thus, the formation of polar, yet atomically dense $\{111\}$ exposed surfaces is strongly enhanced during the thermal oxidation of metallic Ni at 1400 °C and under poor oxidation conditions. The appearance of either pits or terraces is determined by the general orientation of the grain, with pits developing on $\{100\}$ grains and terraces appearing on grains with other orientations. While sample #800 shows no preferential crystalline planes exposed to the surface due to its polycrystalline nature and poorly faceted grains, the exposed surfaces of sample #1400 are highly oriented parallel to the $\{111\}$ crystallographic planes, even if the general texture shows a preferential $\{100\}$ orientation.

In order to further characterize the surface of the samples, XPS measurements were performed on both samples. Fig. 3a shows a XPS micrograph of sample #1400, acquired with the Ni (3p) signal, where three different regions can be recognized. The top left region (B) corresponds to a pitted area, the lower region (C) is a terraced surface, and the top right region (A) is a smooth surface, with no apparent terraces or pits. Fig. 3b – d show a comparison of the O (1s) and Ni (3p) core level and valence band (VB) normalized XPS spectra measured at the three regions of sample #1400 shown in Fig. 3a, and the spectra recorded from sample #800.

It is interesting to note that the spectra recorded from the smooth region in sample #1400 (point A) closely resembles the features observed in sample #800, which is an indication that this area could exhibit similar random orientation, i.e., other than $\{111\}$, as in sample #800. Points B and C, on the other hand, are closer in their recorded

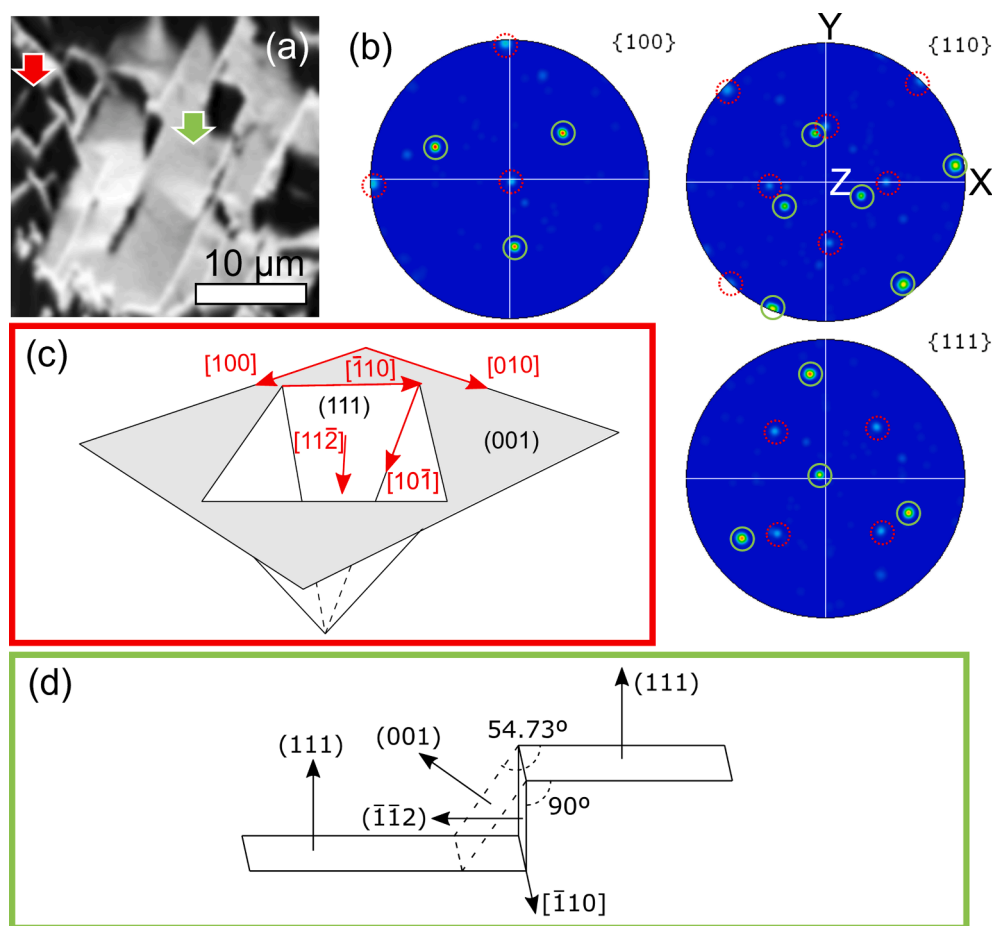


Fig. 2. (a) Detailed SEM micrograph from sample #1400 showing both pits and terraces, and (b) corresponding pole figures in stereographic projection of their crystalline orientations as measured by EBSD. Dashed red circles in (b) correspond to identified poles of the pits, marked by the leftmost red arrow in (a), while solid green circles indicate poles obtained from the terraces marked by the rightmost green arrow in (a). (c) and (d) show schematics of the crystallographic orientations of both pits and terraces.

spectra, which is in agreement with their similarly exposed {111} orientation, as revealed by EBSD. The O (1 s) core level spectrum of sample #800 (Fig. 3b) shows an almost single peak centered at a binding energy (BE) of 531.5 eV, which is related to oxygen in NiO atomic positions. Sample #1400, on the other hand, shows a similar dominant peak in all three spectra, but with a small shoulder at higher BE which can be fitted to a second contribution centered at 533.2 eV related to adsorbed oxygen species. This contribution is almost negligible at the point of random orientation (point A) but becomes significant at points B and C which correspond to {111} surfaces, revealing a preferential absorption of oxygen species on {111} surfaces. Signal from Ni (3p) core level also shows some subtle differences between analyzed regions. This spectrum is composed of two doublets corresponding to Ni (3p_{3/2}) and Ni (3p_{1/2}) levels for both Ni²⁺ and Ni³⁺ oxidation states. The dominant peak is related to the Ni²⁺ doublet centered at 68.6 and 70.1 eV respectively, while the high energy shoulder is produced by the Ni³⁺ doublet centered at 72.0 and 74.9 eV. Due to the energy proximity and identical elemental origin of both contributions, the Ni³⁺ to Ni²⁺ concentration ratio can be estimated from their fitted peak areas. Table 1 summarizes the calculated ratios as well as other quantitative and qualitative parameters measured at each point in Fig. 3a. It is evident from the table that the ratio of Ni³⁺ to Ni²⁺ is similar in both the sample #800 and the randomly oriented surface of point A in sample #1400, while decreases in those surfaces with {111} orientation (terraces and pits), of points B and C.

Fig. 3d shows the measured VB photoelectron spectra in both samples. The VB edge of NiO has two components from O (2p) and Ni (3d) core levels, marked in the spectra. Their relative contribution varies significantly depending on their orientation. Surfaces with random orientation (such as point A in sample #1400 and sample #800) show a

higher contribution from O (2p) core level, compared to {111} surfaces (points B and C in sample #1400), which is in agreement with the lower Ni³⁺ signal observed from {111} surfaces, as higher oxidation states are enhanced by the presence of more oxygen ions in the lattice. The Fermi level, relative to the VB maximum, has been determined from a linear fit of the VB onset, and the results are summarized in Table 1. Both samples show a clear p-type character, as expected, with the Fermi level closer to the VB on {111} surfaces compared to randomly oriented surfaces. While the reduced amount of Ni³⁺ at the {111} surfaces might seem contradictory with their higher p-type character, it is important to remember that these surfaces also showed a significantly higher amount of adsorbed oxygen species that tend to trap electrons from the sample surface, thus reducing their Fermi level, in agreement with the observed results.

The gas sensing properties of both #800 and #1400 samples have been tested upon ethanol exposure at different working temperatures. Fig. 4a shows the sensitivity of both samples to ethanol during three continuous exposure cycles at 28 °C. Sample #800 shows a resistance decrease upon ethanol exposure, while sample #1400 presents a complex behavior, with a fast initial resistance drop followed by a slower increase after a few seconds. The sensitivity of sample #1400 is clearly lower (in absolute value) than that of sample #800 and it degrades visibly at the third cycle. Decreasing the amount of injected ethanol resulted in a lower response, but with no further change in the response curves (not shown).

Ethanol is usually regarded as a reducing agent as it tends to donate electrons through its chemical decomposition at the sensor surface, commonly following the reaction shown in equation (1). For p-type materials as NiO this reaction should lead to an increase in their resistance, as reported previously by several authors [20,23]. However,

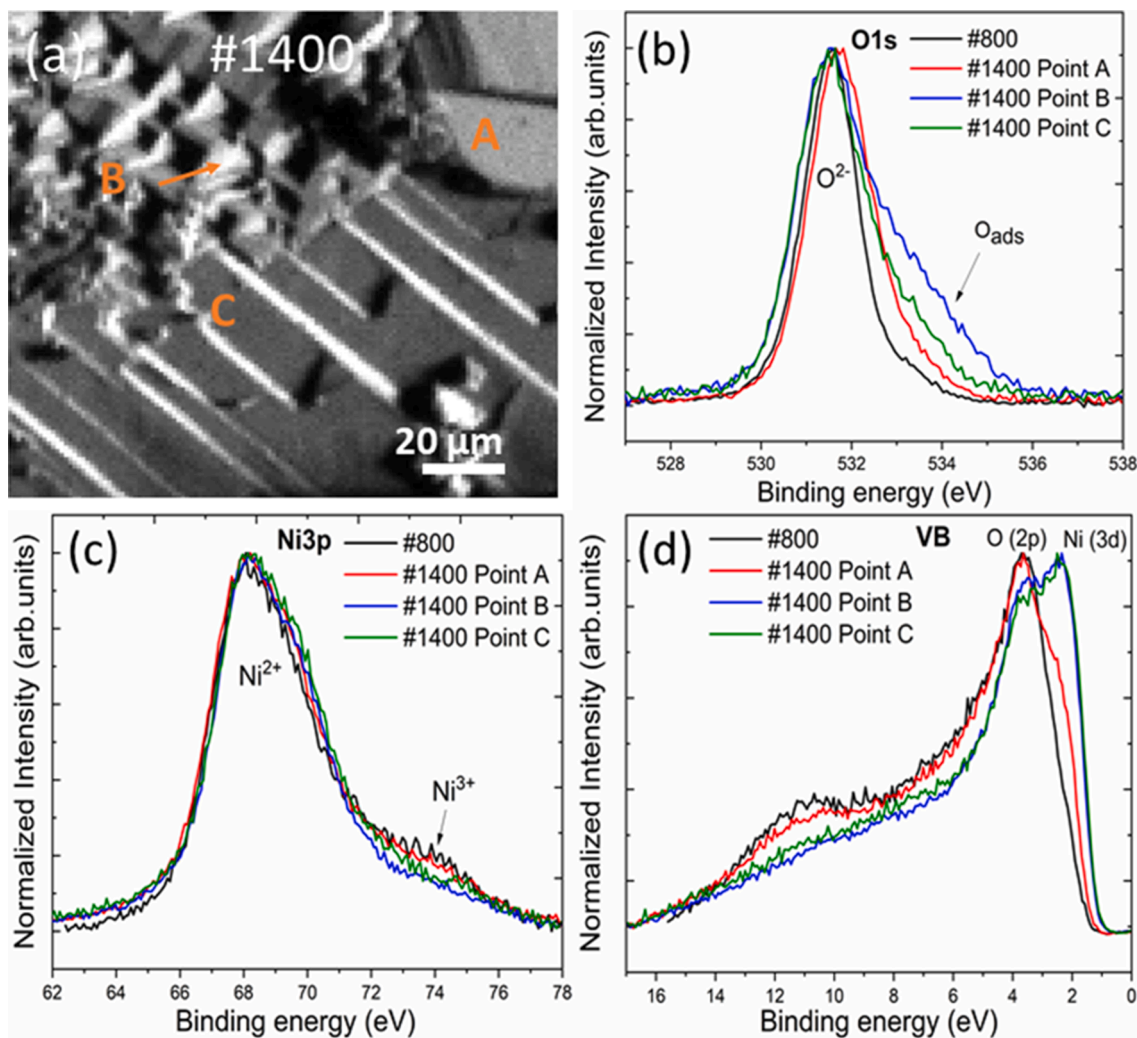


Fig. 3. Representative X-ray photoelectron image (a) of sample #1400 acquired with the Ni (3p) signal, and comparison of the spectra of O (1s) and Ni (3p) core levels (b and c), and valence band (VB) (d) measured at the indicated points in (a), along with the corresponding spectra of sample #800.

Table 1

Qualitative and quantitative XPS results obtained at sample #800 and different points of sample #1400.

Sample	Ads. O	Ni ³⁺ /Ni ²⁺	O(2p)/Ni(3d)	E _F (eV)*
#800	--	0.36	++	1.48
Point A	-	0.34	+	1.37
Point C	+	0.25	-	1.15
Point B	++	0.22	--	1.15

* The Fermi level (E_F) is given relative to the VB maximum.

sample #800 shows an opposite, anomalous behavior, more characteristic of n-type materials. Similarly, sample #1400 presents an initial anomalous resistance drop, followed by the expected resistance increase characteristic of p-type materials exposed to reducing agents. Despite the Fermi level of sample #800 is higher than for sample #1400 (owing to its random orientation nature), both samples are undoubtedly p-type, as the Fermi energy is far closer to the valence band than to the conduction band in both cases, as XPS data indicate.

An inversion from p to n (or n to p) type response has been reported previously for several sensor-analyte pairs, where the n or p type here is referred only to the response to the analyte and not to the conductivity type (electrons or holes). The mechanisms behind this phenomenon are usually not well understood and tend to be peculiar of each sensor-analyte system, without a general theory describing the majority of

the cases. For instance an anomalous NiO response to H₂S has been reported to be caused by the partial reaction of H₂S with NiO to form NiS, which is more conductive [29]. Indium oxide nanowires show a different response to NH₃ depending on the position of their Fermi level relative to the charge neutrality level of the adsorbed NH₃ behaving as n-type for highly doped In₂O₃ and as p-type for more intrinsic samples [9]. Other authors have reported a switch from n to p response on Fe₂O₃ towards NO₂ depending on the NO₂ concentration and sensing temperature caused by two competitive processes, namely the competition between NO₂⁻ and O⁻ species for the same adsorption sites, and the chemical reaction of adsorbed NO₂⁻ and O⁻ to form gaseous NO and O₂ [14]. However, to the best of our knowledge no anomalous sensing behavior has been reported so far for the NiO-ethanol sensing pair.

To shed some light on this abnormal behavior we have performed sensing measurements at higher operation temperatures, while maintaining the same ethanol concentration. Fig. 4b shows the sensing response of sample #800 at room temperature (28 °C) and at 50 and 100 °C, characterized by a slight sensitivity increase at higher temperatures. At 50 °C the response curve (i.e., the region where ethanol is introduced) shows a slight inversion in its trend after reaching the saturation value. At 100 °C this inversion in the response becomes evident, with a resistance increase appearing shortly after the ethanol has been introduced, very similar to the response characteristics of sample #1400 at RT. For sample #1400 the situation is completely

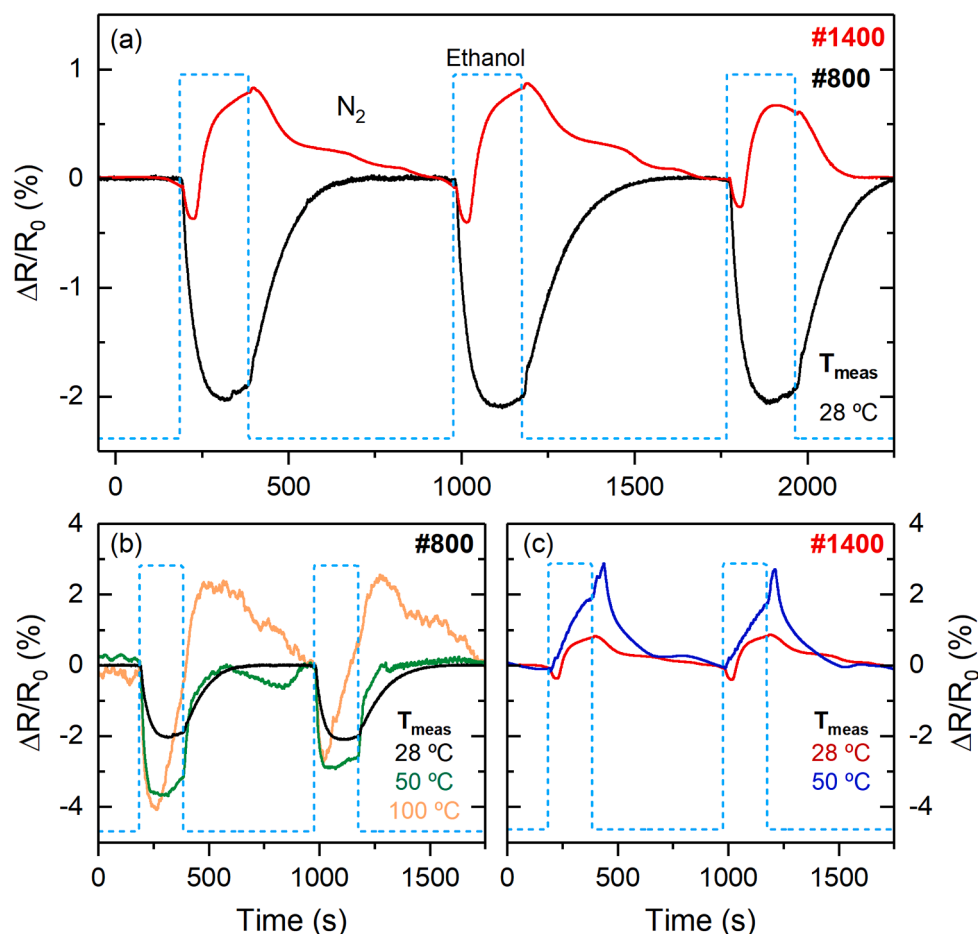


Fig. 4. Conductometric gas response to the presence of a high concentration of ethanol ($\sim 16,000$ ppm), for samples #800 and #1400. (a) Comparison between both samples measured at room temperature. (b) Gas response of sample #800 measured at different temperatures up to 100 °C. (c) Gas response of sample #1400 measured at 28 °C and 50 °C.

different (Fig. 4c). At 50 °C the sensitivity increases by a factor 2 and, while the anomalous part of the response curve disappears almost completely at this temperature, it shows an enhanced signal at the beginning of the recovery curve (i.e., the region where ethanol is evacuated). Moreover, the sensitivity degradation is already visible in the second cycle, in contrast to the case at RT where it was apparent only at the third cycle. Interestingly at 100 °C the sensitivity of the sample drops to almost zero (not shown), showing nothing more than a very noisy signal.

Another interesting feature of these sensitivity curves is the fast response/recovery times shown by the anomalous behavior. In order to accurately measure these values, the sensitivity curves have been fitted to two exponentials, corresponding to the response and recovery parts for each cycle. Table 2 shows the obtained values for sample #800 at each temperature. At 100 °C the appearance of the complex dual behavior prevents the determination of the recovery time and thus only the response time for the initial fast resistance drop, corresponding to the anomalous mechanism, has been estimated. It is clear that not only the sensitivity of sample #800 increases with temperature, but also the response and recovery times decrease, as expected, although the recovery time seems to reach a minimum value at a 50 °C. For sample #1400 its complex behavior hinders any fit to a simple exponential trend, and thus no quantitative analysis may be performed; however, it is clear from the graphs that the response and recovery times are significantly larger compared to sample #800. Comparison with values published in previous works (Table 2) highlight the fast kinetics of the

Table 2

Response and recovery times measured at different temperatures for sample #800 and comparison with previous works at high temperature.

Sample type	T (°C)	τ_{response} (s)	τ_{recovery} (s)	Reference
Ceramic pellet	28	30.34 ± 0.14	86.8 ± 0.4	This work
Ceramic pellet	50	14.32 ± 0.08	39.8 ± 0.6	This work
Ceramic pellet	100	16.0 ± 0.3	–	This work
Al doped NiO nanorod	200	48	40	[30]
NiO Nanoparticles	250	4	8	[31]
NiO Microrods	250	15	25	[32]
NiO nanosheets	300	27–48	77–105	[12]
NiO/ZnO nanowires	300	4	28	[33]
NiO-SnO ₂ nanofibers	300	2	3	[24]
NiO Nanowires	340	17	15	[21]
NiO porous sphere	350	23	24	[34]
NiO Nanoparticles	350	124	–	[35]
In ₂ O ₃ -Decorated NiO Hollow Nanostructures	325–475	60–150	23–90	[23]

anomalous response, which show similar performances than samples measured at high temperature (>200 °C).

These results suggest the presence of two dominant and competitive mechanisms with opposite influence on the sample sensitivity: one responsible for the expected p-type behavior, and another one leading to an apparent abnormal n-type behavior. The normal behavior can be attributed to the dissociative chemisorption of ethanol at the surface of

the sample and subsequent electron release via reaction (1) or any other equivalent reaction involving adsorbed oxygen species, commonly reported in the literature [12,20–26]. The anomalous behavior, on the contrary, cannot be explained by this mechanism, so we propose a process in which NiO electrons are trapped by physisorbed or non-dissociative chemisorbed ethanol molecules, leading to a resistance decrease upon ethanol exposure. Chemical reactions as well as dissociative chemisorption usually involve higher energy barriers compared to physisorption and non-dissociative chemisorption, which usually present smaller or negligible energy barriers. Thus, the normal p-type response may increase significantly at higher temperatures, while the anomalous mechanism is more temperature insensitive, explaining why at higher temperatures the behavior of both samples is dominated by the expected p-type response, even if for sample #800 the anomalous mechanism is more relevant at room temperature. It also explains why at 50 °C the sensitivity improvement of sample #1400 is larger than that of sample #800. Larger energy barriers also imply slower kinetics, as observed from the qualitative comparison of the response time in both samples, where the anomalous behavior shows faster kinetics compared to the normal p-type behavior at any temperature.

There are still couple of questions remaining, which are the passivation of sample #1400 at 100 °C, and more importantly, the origin of the different behavior between both samples. The first question may be answered considering a surface poisoning process, consistent with the degradation of the response after one or two cycles, depending on the sensing temperature. Ethanol decomposition may produce a series of different subproducts which, owing to the relatively low temperature of the sensing experiments, may desorb slowly from the surface, limiting the number of adsorption sites for new ethanol molecules over time. Thus, as more cycles are measured, more subproduct molecules get attached to the surface, degrading the response. At higher temperatures ethanol is decomposed more efficiently, but if these temperatures are not high enough (typically 200–300 °C) the resulting subproducts may remain on the surface for long periods of time, thus accelerating the poisoning process and explaining the faster degradation in the response of sample #1400 at 50 °C and its passivation at 100 °C. The response of sample #800 is dominated by physisorption/non-dissociative chemisorption processes at room temperature, and therefore should not be affected by surface poisoning at this temperature. However, at higher temperatures, when ethanol decomposition becomes more relevant, the response starts degrading already during the second cycle, at both 50 °C but more significantly at 100 °C, as shown in Fig. 4b. In this case, the degradation is observed mainly in the dominant anomalous response, strongly pointing to the blockage of the active ethanol adsorption sites as the main poisoning source, rather than other possible processes such as the depletion of the adsorbed oxygen, necessary for the normal p-type response, but more irrelevant for the anomalous response. The observed poisoning is not irreversible, and recovers after several hours at room temperature, as expected from the formation of slow desorbing subproducts.

Regarding the rather different response observed in both samples, there are essentially four main differences between both samples: grain size/boundaries, porosity, grain orientation, and surface oxidation state/defects. Grain size and grain boundary density are interrelated magnitudes and may play a role in the sensing process through two possible mechanisms. The first one is related to the presence of energy barriers in the conduction path due to the formation of depletion layers at the grain boundaries. The barrier height, and hence the sample conductivity, is then controlled by the injection/extraction of charge produced by the adsorbed molecules [10]. Therefore, under this mechanism a change in grain size would change the sensitivity of the sample, but not the type of response, i.e. n- or p-type. The second mechanism arises when the grain size is reduced close to the Debye length of the material [36]. Charge injection/extraction may induce the formation of an inversion layer whose size is proportional to the Debye length. If the grain size is small enough, the intragrain conduction is controlled by the

inversion layer and the material behaves as the opposite type. While this may explain the change from p-type to n-type sensitivity on sample #800, the average grain size of this sample is of several microns. To achieve Debye lengths of this magnitude at room temperature a carrier density as low as 10^{12} cm^{-3} would be required, which is not compatible with its pronounced p-type character, as observed by XPS, and relatively high conductivity. Porosity may influence the diffusion speeds into the bulk of the samples and should affect mainly to the recovery and response times, but should not significantly affect the physicochemical processes leading to the sensing response. Even if porosity is quite different between both samples, a qualitative comparison of the response and recovery times for the same sensing mechanism (either normal p-type or anomalous) shows similar behaviors in both samples. Moreover, experiments performed on samples fabricated at intermediate temperatures, showing significantly lower porosity and higher grain size than sample #800 (close to those of sample #1400), but similar random exposed surface orientation, show similar behaviors as sample #800. Conversely, partially textured samples present intermediate behaviors between samples #800 and #1400 (see Supporting Information S2), despite having a similar grain size as sample #1400. Therefore, porosity and/or grain size/boundaries do not seem to determine the type of sensing response obtained in the samples.

XPS results revealed a small increase in the $\text{Ni}^{3+}/\text{Ni}^{2+}$ ratio in sample #800 compared to sample #1400. However, this difference seems to be more related to the predominant orientation of the exposed surface rather than the treatment temperature, as only grains with {111} exposed surfaces in sample #1400 show a significantly smaller $\text{Ni}^{3+}/\text{Ni}^{2+}$ ratio compared to sample #800. Thus, oxidation state is directly related to the crystalline orientation of the exposed surface. A change in the $\text{Ni}^{3+}/\text{Ni}^{2+}$ ratio could affect the adsorption and subsequent decomposition of ethanol at the surface, as well as the amount of adsorbed oxygen species, involved in the normal p-type response. Oxygen indeed adsorbs less efficiently on sample #800 and randomly oriented surfaces of sample #1400 as compared to {111} exposed surfaces (see Table 1 and Fig. 3b). In fact, grain orientation alone is sufficient to induce significant changes in the gas sensing response of NiO. Polar NiO {111} surfaces are known to be more chemically active than other low Miller index, non-polar surfaces such as {100} or {110} [37]. Predominance of {111} surfaces in NiO may significantly enhance the decomposition rate of ethanol even at low temperatures, as observed on sample #1400, while other orientations may favor adsorption and charge transfer/trapping processes over chemical reactions.

To further confirm this hypothesis, DFT calculations of ethanol adsorption over different surfaces have been performed. Fig. 5 shows a side view of the room temperature equilibrium position of the ethanol molecule on top of {100}, {110} and Ni- or O- terminated {111} surfaces. The corresponding calculated density of states (DOS) for each situation is shown in Fig. S3 in the Supporting Information. In order to simplify the interpretation of the results no amount of Ni^{3+} ions was considered in this case. For the polar surfaces the most stable octopolar surface reconstruction was used [38]. It is evident from the calculations that both Ni-{111} and O-{111} polar surfaces as well as {110} non-polar surface induce the decomposition of the ethanol molecule by breaking one H-O or C-H bond. The released hydrogen atom may either inject one electron to the NiO surface or combine with an adsorbed O to eventually form an H_2O molecule, which can desorb from the surface, releasing a trapped electron. Conversely, {100} surface shows no catalytic activity, leading only to the adsorption of ethanol on top of a surface Ni atom.

Charge transfer has also been calculated for each case by comparing the total amount of electrons per atom at the surface and at the ethanol molecule before and after being adsorbed/decomposed. Table 3 shows the total charge transfer for each surface, with negative values being electrons transferred from the NiO surface to the ethanol molecule.

It is clear that ethanol tends to trap electrons from the surface of NiO irrespective of its orientation. Similar behavior has been reported for

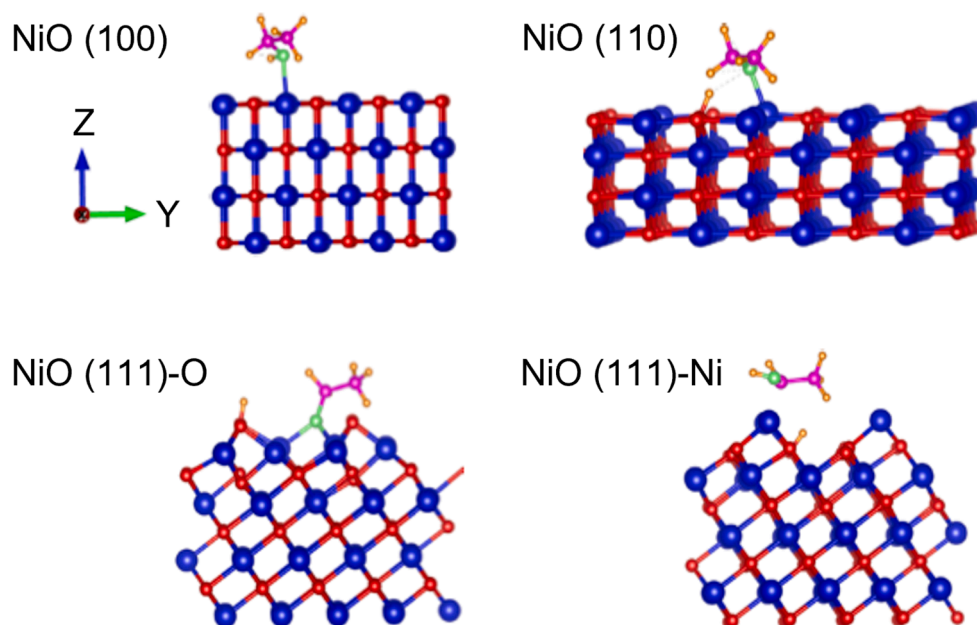


Fig. 5. DFT calculations for the adsorption of a single ethanol molecule atop of different NiO crystalline surfaces, comprising {100}, {110} and nickel or oxygen terminated {111} surfaces, showing the final stable configuration of adsorbed ethanol.

Table 3

Charge transfer, q , upon ethanol adsorption on different NiO surfaces.

Surface	{100}	{110}	Ni-{111}	O-{111}
Transferred q^*	-0.11	-0.43	-0.09	-0.36

* Negative values imply an electron transfer from NiO surface to ethanol molecule.

ethanol adsorption on CaO which is also a p-type semiconductor [39]. Therefore, ethanol adsorption alone, should always lead to a decrease in resistance on NiO, which opposes to the resistance increase caused by reaction (1) that takes place on some surfaces after the ethanol molecule has been decomposed.

These results strongly support the hypothesis of the coexistence of, at least, two main competing sensing mechanisms that takes place at the same time during ethanol sensing at room temperature. One mechanism would be based on the dissociative chemisorption of ethanol, which is particularly efficient on {110} and {111} surfaces such as those predominating on sample #1400, and another one based on charge

transfer/trapping of adsorbed ethanol, which is produced on every surface regardless of its orientation. A schematic of both proposed processes is shown in Fig. 6.

It is worth noting that dissociative adsorption of ethanol on {110} and {111} NiO surfaces obtained by DFT calculations results from energy minimization of the final state of the system, and thus no energy barrier or other kinetic limitations are considered. Chemical dissociation is usually an energy activated process and surface catalyzed dissociation enhances these reactions by lowering the total energy barrier of the process. Therefore, higher temperatures should enhance the normal p-type response by speeding up the dissociation processes. On samples showing random orientations such as sample #800 or sample #1150 in the Supporting Information, the absence of a preferential orientation of the exposed surfaces along {110} or {111} planes strongly decreases the efficiency at which ethanol is decomposed. Thus, the anomalous response dominates in these samples even at high temperatures, with the normal p-type response only slightly starting to show up at temperatures of at least 100 °C. On the contrary, for samples with {111} preferential orientation the dissociation process is strongly favored and normal p-

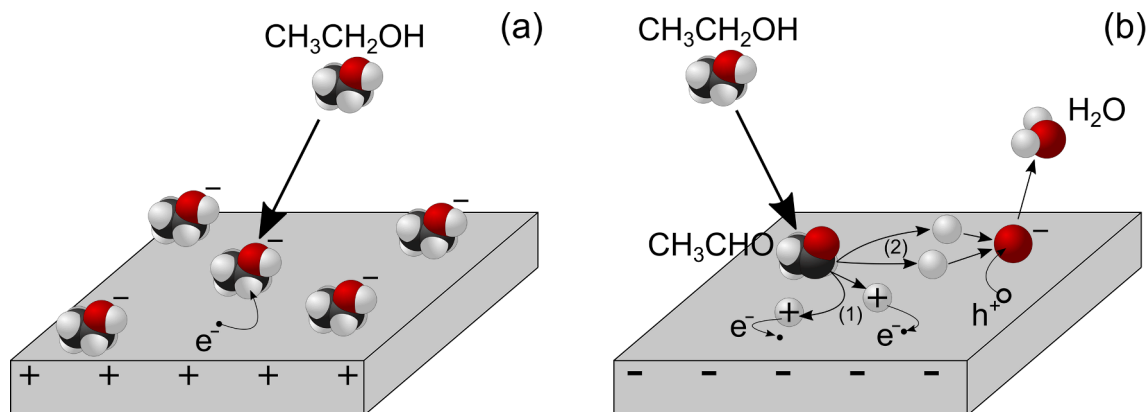


Fig. 6. Schematic of the proposed competing ethanol sensing mechanism on NiO. (a) Anomalous sensing mechanism: ethanol molecules adsorb over the NiO surface, acting as electron traps/acceptors, increasing the overall conductivity of the sample. (b) Normal p-type sensing mechanism: ethanol molecules dissociate on the NiO surface, oxidizing and releasing H atoms. These H atoms may either inject directly electrons to the surface (pathway 1), or recombine with adsorbed O ions to form H₂O, releasing a trap electron (pathway 2).

type response is the relevant mechanism even at room temperature (or in the case of sample #1350 in the [Supporting Information](#), at higher temperatures due to its more incomplete surface texture). If the desorption rate of decomposed ethanol subproducts or their complete decomposition into CO₂ and H₂O is too slow, compared to the speed at which they are produced, surface poisoning takes place, degrading the sensing response. This could explain the poisoning effect observed on sample #1400 working at high temperature below 200 °C, which is the normal operation temperature of NiO ethanol sensors.

The anomalous sensing response of NiO to ethanol has been commonly overlooked due to the fact that these sensors usually work at higher sensing temperatures, typical of conductometric sensors. Thus, this work emphasizes the importance of studying the conductometric sensing response of different semiconductor systems also at lower temperatures, even down to room temperature. An important feature of the anomalous response, besides its different physicochemical nature, is actually its fast response at such low temperatures. Response and recovery times are important parameters in the performance of any gas sensor. Considering the room temperature operation and ceramic nature of the samples, both values are surprisingly low, comparable to other reports in the literature measured at high temperature and with optimized sample morphologies, as shown in [Table 2](#). One has to bear in mind that high sensing temperatures are usually employed not only to improve the sensitivity of the devices, but more importantly to reduce their response and recovery times to values actually usable in real applications. This higher operation temperature requires a constant source of heat, which in turn imposes a limit to the minimum power consumption of the device, usually requiring the access to a constant source of power supply such as the power grid. Room temperature operation might actually overcome this limitation by considerably reducing the power consumption, allowing an effective operation on regular batteries. Even though the sensitivity is not very high, the anomalous response showed higher sensitivities at room temperature than the normal p-type response and should improve significantly by reducing the bulk to surface ratio, as usually observed in thin and nanoparticle films.

4. Conclusions

To summarize, the sensing response of polycrystalline p-type NiO samples to ethanol at room temperature has been studied as a function of their microstructure and preferential orientation of their exposed surfaces. It is found that samples with no texture present a fast anomalous resistance decrease when exposed to ethanol, similar to what would be expected on n-type materials. Conversely, samples strongly texturized along {111} planes show a much slower normal p-type response consisting in a resistance increase after being exposed to ethanol. Both responses are produced by the competition of two opposing mechanisms, which has been attributed to an electron transfer process from the sample to the adsorbed ethanol molecule for the anomalous response, and to a catalytic decomposition of the ethanol molecule and subsequent reaction with adsorbed O species for the normal p-type response. The slower catalytic decomposition is enhanced on {111} surfaces and at high temperatures, while the faster electron transfer is favored at lower temperatures on randomly oriented surfaces. Therefore, NiO gas sensing mechanisms can be modulated by selecting different morphologies and/or surface preferential orientations, which can be tuned by selecting the appropriate experimental conditions. More importantly, it is shown that fast ethanol gas sensing response and recovery times can be achieved at room temperature on NiO provided that electron transfer is the dominant sensing mechanism. Similar competing mechanisms are expected to be present in other sensor-analyte systems, which opens the door for lower power consumption sensor devices operating at room temperature.

CRediT authorship contribution statement

Javier Bartolomé: Conceptualization, Investigation, Formal analysis, Writing – original draft, Writing – review & editing, Visualization, Supervision, Project administration, Funding acquisition. **María Taño:** Investigation, Formal analysis, Writing – original draft, Writing – review & editing, Visualization. **Ruth Martínez-Casado:** Investigation, Writing – review & editing, Visualization. **David Maestre:** Conceptualization, Writing – review & editing, Data curation, Supervision. **Ana Cremades:** Conceptualization, Writing – review & editing, Supervision, Project administration, Funding acquisition.

Declaration of Competing Interest

The authors declare that they have no known competing financial interests or personal relationships that could have appeared to influence the work reported in this paper.

Acknowledgments

This work was supported by the V-PRICIT of Comunidad de Madrid through the research project PR65/19-22335 and by the RTI2018-097195-B-I00 project supported by MCI/AEI/FEDER, UE. Authors thank the ESCA-microscopy staff at the Elettra Synchrotron for their help during XPS and additional sensitivity measurements. J.B. acknowledges financial support from the Comunidad de Madrid through the Talento fellowship 2017-T2/IND-5617.

Appendix A. Supplementary material

Electronic [supplementary information](#) available: sensing setup (S1), additional measurements with samples having intermediate microstructure (S2), density of states (DOS) of the different surfaces before and after ethanol adsorption calculated by DFT (S3).

Supplementary data to this article can be found online at <https://doi.org/10.1016/j.apsusc.2021.152134>.

References

- [1] P.T. Moseley, Progress in the development of semiconducting metal oxide gas sensors: A review, *Meas. Sci. Technol.* 28 (8) (2017) 082001, <https://doi.org/10.1088/1361-6501/aa7443>.
- [2] G.W. Hunter, S. Akbar, S. Bhansali, M. Daniele, P.D. Erb, K. Johnson, C.-C. Liu, D. Miller, O. Oralkan, P.J. Hesketh, P. Manickam, R.L. Vander Wal, Editors' Choice—Critical Review—A Critical Review of Solid State Gas Sensors, *J. Electrochem. Soc.* 167 (2020) 037570, <https://doi.org/10.1149/1945-7111/ab729c>.
- [3] G. Korotcenkov, V. Brinzari, B.K. Cho, In₂O₃- and SnO₂-Based Thin Film Ozone Sensors: Fundamentals, *J. Sensors*. 2016 (2016) 1–31, <https://doi.org/10.1155/2016/3816094>.
- [4] C.Y. Wang, V. Cimalla, T. Kups, C.C. Röhlig, T. Stauden, O. Ambacher, M. Kunzer, T. Passow, W. Schirmacher, W. Pletschen, K. Köhler, J. Wagner, Integration of In₂O₃ nanoparticle based ozone sensors with GaInN/GaN light emitting diodes, *Appl. Phys. Lett.* 91 (2007) 103509, <https://doi.org/10.1063/1.2779971>.
- [5] C. Baratto, E. Comini, G. Faglia, G. Sberveglieri, M. Zha, A. Zappettini, Metal oxide nanocrystals for gas sensing, *Sensors Actuators, B Chem.* 109 (1) (2005) 2–6, <https://doi.org/10.1016/j.snb.2005.03.091>.
- [6] N.S. Ramgir, Y. Yang, M. Zacharias, Nanowire-based sensors, *Small*. 6 (16) (2010) 1705–1722, <https://doi.org/10.1002/smll.201000972>.
- [7] J.-E. Haugen, O. Tomic, K. Kvaal, A calibration method for handling the temporal drift of solid state gas-sensors, *Anal. Chim. Acta*. 407 (1–2) (2000) 23–39, [https://doi.org/10.1016/S0003-2670\(99\)00784-9](https://doi.org/10.1016/S0003-2670(99)00784-9).
- [8] J. Zhang, X. Liu, G. Neri, N. Pinna, Nanostructured Materials for Room-Temperature Gas Sensors, *Adv. Mater.* 28 (5) (2016) 795–831, <https://doi.org/10.1002/adma.201503825>.
- [9] D. Zhang, C. Li, X. Liu, S. Han, T. Tang, C. Zhou, Doping dependent NH₃ sensing of indium oxide nanowires, *Appl. Phys. Lett.* 83 (9) (2003) 1845–1847, <https://doi.org/10.1063/1.1604194>.
- [10] C.Y. Wang, V. Cimalla, T. Kups, C.C. Röhlig, H. Romanus, V. Lebedev, J. Pezoldt, T. Stauden, O. Ambacher, Photoreduction and oxidation behavior of In₂O₃ nanoparticles by metal organic chemical vapor deposition, 044310-044310–6, *J. Appl. Phys.* 102 (2007), <https://doi.org/10.1063/1.2770831>.

- [11] A. Gurlo, N. Bárson, A. Oprea, M. Sahn, T. Sahn, U. Weimar, An n- to p-type conductivity transition induced by oxygen adsorption on α -Fe₂O₃, *Appl. Phys. Lett.* 85 (12) (2004) 2280–2282, <https://doi.org/10.1063/1.1794853>.
- [12] C. Zhao, J. Fu, Z. Zhang, E. Xie, Enhanced ethanol sensing performance of porous ultrathin NiO nanosheets with neck-connected networks, *RSC Adv.* 3 (2013) 4018–4023, <https://doi.org/10.1039/c3ra23182h>.
- [13] S. Sänze, C. Hess, Ethanol gas sensing by indium oxide: An operando spectroscopic Raman-FTIR study, *J. Phys. Chem. C* 118 (44) (2014) 25603–25613, <https://doi.org/10.1021/jp509068s>.
- [14] Z. Dai, C.-S. Lee, Y. Tian, I.-D. Kim, J.-H. Lee, Highly reversible switching from P- to N-type NO₂ sensing in a monolayer Fe₂O₃ inverse opal film and the associated P-N transition phase diagram, *J. Mater. Chem. A* 3 (7) (2015) 3372–3381, <https://doi.org/10.1039/C4TA05438E>.
- [15] S. Roso, D. Degler, E. Llobet, N. Barsan, A. Urakawa, Temperature-Dependent NO₂ Sensing Mechanisms over Indium Oxide, *ACS Sensors* 2 (9) (2017) 1272–1277, <https://doi.org/10.1021/acssensors.7b00504>.
- [16] G. Korotcenkov, V. Brinzari, V. Golovanov, A. Cerneavski, V. Matolin, A. Tadd, Acceptor-like behavior of reducing gases on the surface of n-type In₂O₃, *Appl. Surf. Sci.* 227 (1–4) (2004) 122–131, <https://doi.org/10.1016/j.apsusc.2003.11.051>.
- [17] E. Comini, Metal oxide nano-crystals for gas sensing, *Anal. Chim. Acta* 568 (1–2) (2006) 28–40, <https://doi.org/10.1016/j.aca.2005.10.069>.
- [18] A. Dey, Semiconductor metal oxide gas sensors: A review, *Mater. Sci. Eng. B Solid-State Mater. Adv. Technol.* 229 (2018) 206–217, <https://doi.org/10.1016/j.mseb.2017.12.036>.
- [19] H.-J. Kim, J.H. Lee, Highly sensitive and selective gas sensors using p-type oxide semiconductors: Overview, *Sensors Actuators, B Chem.* 192 (2014) 607–627, <https://doi.org/10.1016/j.snb.2013.11.005>.
- [20] T.P. Mokoena, H.C. Swart, D.E. Motaung, A review on recent progress of p-type nickel oxide based gas sensors: Future perspectives, *J. Alloys Compd.* 805 (2019) 267–294, <https://doi.org/10.1016/j.jallcom.2019.06.329>.
- [21] J. Wei, X. Li, Y. Han, J. Xu, H. Jin, D. Jin, X. Peng, B.o. Hong, J. Li, Y. Yang, H. Ge, X. Wang, Highly improved ethanol gas-sensing performance of mesoporous nickel oxides nanowires with the stannum donor doping, *Nanotechnology* 29 (24) (2018) 245501, <https://doi.org/10.1088/1361-6528/aab9d8>.
- [22] M. Taño, D. Maestre, A. Cremades, Fabrication and study of self-assembled NiO surface networks assisted by Sn doping, *J. Alloys Compd.* 827 (2020) 154172, <https://doi.org/10.1016/j.jallcom.2020.154172>.
- [23] H.-J. Kim, H.-M. Jeong, T.-H. Kim, J.-H. Chung, Y.C. Kang, J.-H. Lee, Enhanced ethanol sensing characteristics of In₂O₃-decorated NiO hollow nanostructures via modulation of hole accumulation layers, *ACS Appl. Mater. Interfaces* 6 (20) (2014) 18197–18204, <https://doi.org/10.1021/am5051923>.
- [24] L. Liu, S. Li, L. Wang, C. Guo, Q. Dong, W. Li, Enhancement ethanol sensing properties of NiO-SnO₂ nanofibers, *J. Am. Ceram. Soc.* 94 (2011) 771–775, <https://doi.org/10.1111/j.1551-2916.2010.04137.x>.
- [25] G. Niu, C. Zhao, H. Gong, Z. Yang, X. Leng, F. Wang, NiO nanoparticle-decorated NiO₂ nanosheets for ethanol sensing with enhanced moisture resistance, *Microsystems Nanoeng.* 5 (2019) 21, <https://doi.org/10.1038/s41378-019-0060-7>.
- [26] D. Li, Y. Zhang, D. Liu, S. Yao, F. Liu, B. Wang, P. Sun, Y. Gao, X. Chuai, G. Lu, Hierarchical core/shell ZnO/NiO nanoheterojunctions synthesized by ultrasonic spray pyrolysis and their gas-sensing performance, *CrystEngComm* 18 (41) (2016) 8101–8107, <https://doi.org/10.1039/C6CE01621A>.
- [27] M. Taño, J. Bartolomé, L. Gregoratti, P. Modrzynski, D. Maestre, A. Cremades, Self-Organized NiO Microcavity Arrays Fabricated by Thermal Treatments, *Cryst. Growth Des.* 20 (6) (2020) 4082–4091, <https://doi.org/10.1021/acs.cgd.0c00365>.
- [28] R. Dovesi, A. Erba, R. Orlando, C.M. Zicovich-Wilson, B. Civalieri, L. Maschio, M. Rérat, S. Casassa, J. Baima, S. Salustro, B. Kirtman, Quantum-mechanical condensed matter simulations with CRYSTAL, *Wiley Interdiscip. Rev. Comput. Mol. Sci.* 8 (4) (2018), <https://doi.org/10.1002/wcms.2018.8.issue-4>.
- [29] S.K. Ganapathi, M. Kaur, R. Singh, V.I. Singh, A.K. Debnath, K.P. Muthe, S. C. Gadkari, Anomalous Sensing Response of NiO Nanoparticulate Films toward H₂S, *ACS Appl. Nano Mater.* 2 (10) (2019) 6726–6737, <https://doi.org/10.1021/acsnano.9b01637>.
- [30] C. Wang, X. Cui, J. Liu, X. Zhou, X. Cheng, P. Sun, X. Hu, X. Li, J. Zheng, G. Lu, Design of Superior Ethanol Gas Sensor Based on Al-Doped NiO Nanorod-Flowers, *ACS Sensors* 1 (2) (2016) 131–136, <https://doi.org/10.1021/acssensors.5b00123>.
- [31] M. Carbone, P. Tagliatesta, NiO grained-flowers and nanoparticles for ethanol sensing, *Materials (Basel)* 13 (2020) 1880, <https://doi.org/10.3390/MA13081880>.
- [32] Shailja, K.J. Singh, R.C. Singh, Singh, Highly sensitive and selective ethanol gas sensor based on Ga-doped NiO nanoparticles, *J. Mater. Sci. Mater. Electron.* 32 (8) (2021) 11274–11290, <https://doi.org/10.1007/s10854-021-05796-8>.
- [33] S. Zhao, Y. Shen, Y. Xia, A. Pan, Z. Li, C. Carraro, R. Maboudian, Synthesis and gas sensing properties of NiO/ZnO heterostructured nanowires, *J. Alloys Compd.* 877 (2021) 160189, <https://doi.org/10.1016/j.jallcom.2021.160189>.
- [34] C. Nie, W. Zeng, Y. Li, The 3D crystal morphologies of NiO gas sensor and constantly improved sensing properties to ethanol, *J. Mater. Sci. Mater. Electron.* 30 (2) (2019) 1794–1802, <https://doi.org/10.1007/s10854-018-0451-9>.
- [35] V. Kruefu, A. Wisitsoraat, D. Phokharatkul, A. Tuantranont, S. Phanichphant, Enhancement of p-type gas-sensing performances of NiO nanoparticles prepared by precipitation with RuO₂ impregnation, *Sensors Actuators B Chem.* 236 (2016) 466–473, <https://doi.org/10.1016/J.SNB.2016.06.028>.
- [36] J. Liang, Q. Lou, W. Wu, K. Wang, C. Xuan, NO₂ Gas Sensing Performance of a VO₂(B) Ultrathin Vertical Nanosheet Array: Experimental and DFT Investigation, *ACS Appl. Mater. Interfaces* 13 (27) (2021) 31968–31977, <https://doi.org/10.1021/acsaami.1c05251>.
- [37] C. Xu, D.W. Goodman, Structure sensitivity of oxide surfaces: The adsorption and reaction of carbon monoxide and formic acid on NiO(100) and NiO(111), *Catal. Today* 28 (4) (1996) 297–303, [https://doi.org/10.1016/S0920-5861\(96\)00044-2](https://doi.org/10.1016/S0920-5861(96)00044-2).
- [38] A. Wander, I.J. Bush, N.M. Harrison, Stability of rocksalt polar surfaces: An ab initio study of MgO(111) and NiO(111), *Phys. Rev. B - Condens. Matter Mater. Phys.* 68 (2003), 233405, <https://doi.org/10.1103/PhysRevB.68.233405>.
- [39] V. Orazi, A. Juan, E.A. González, J.M. Marchetti, P.V. Jasen, DFT study of ethanol adsorption on CaO(001) surface, *Appl. Surf. Sci.* 500 (2020) 144254, <https://doi.org/10.1016/j.apsusc.2019.144254>.